

Hot-electron influence on L -shell spectra of multicharged Kr ions generated in clusters irradiated by femtosecond laser pulses

S. B. Hansen and A. S. Shlyaptseva

Physics Department/220, University of Nevada, Reno, Nevada 89557

A. Y. Faenov, I. Y. Skobelev, A. I. Magunov, and T. A. Pikuz

Multicharged Ions Spectra Data Center of VNIIFTRI, Mendeleev, Moscow region 141570, Russia

F. Blasco, F. Dorchies, C. Stenz, and F. Salin

CELIA, Universite Bordeaux I, 33405 Talence, France

T. Auguste, S. Dobosz, P. Monot, P. D' Oliveira, and S. Hulin

CEA, Centre D'Etudes de Saclay, DRECAM/SPAM, Bâtiment 522, 91191 Gif-sur-Yvette, France

U. I. Safronova

Department of Physics, University of Notre Dame, Notre Dame, Indiana 46566

K. B. Fournier

Lawrence Livermore National Laboratory, P.O. Box 808, Livermore, California 94550

(Received 7 April 2002; published 17 October 2002)

Strong L -shell x-ray emission has been obtained from Kr clusters formed in gas jets and irradiated by 60–500-fs laser pulses. Spectral lines from the F-, Ne- Na-, and Mg-like charge states of Kr have been identified from highly resolved x-ray spectra. Spectral line intensities are used in conjunction with a detailed time-dependent collisional-radiative model to diagnose the electron distribution functions of plasmas formed in various gas jet nozzles with various laser pulse durations. It is shown that L -shell spectra formed by relatively long nanosecond-laser pulses can be well described by a steady-state model without hot electrons when opacity effects are included. In contrast, adequate modeling of L -shell spectra from highly transient and inhomogeneous femtosecond-laser plasmas requires including the influence of hot electrons. It is shown that femtosecond-laser interaction with gas jets from conical nozzles produces plasmas with higher ionization balances than plasmas formed by gas jets from Laval nozzles, in agreement with previous work for femtosecond laser interaction with Ar clusters.

DOI: 10.1103/PhysRevE.66.046412

PACS number(s): 52.50.Jm, 32.30.Rj, 36.40.Vz, 52.25.Os

I. INTRODUCTION

The interaction of short, high-intensity laser pulses with dense atomic clusters in gas jets has been of much interest in recent years (see, for example, Refs. [1–12]). According to an accepted model of cluster formation, the expansion and cooling of high pressure gas jets in a vacuum permits the formation of near solid-density atomic clusters by Van der Waals forces. When irradiated by the prepulse of a short, high-intensity laser, the dense clusters heat up, ionize, and expand. The rare gas surrounding the clusters is not an effective transmitter of heat, so the clusters retain their energy as they expand. The clusters best absorb the energy of the main laser pulse when the prepulse ionization and expansion collude to form a plasma with an electron density near the critical density for the laser energy. The energy of the main laser pulse is absorbed by the electrons at resonance energies around 3–10 keV. Hot electrons created by the main pulse drive collisional ionization and excitation that result in bright x-ray emission from the clusters. By optimizing the size and density of the clusters and timing their interaction with the laser prepulse and ultrashort (fs) main pulse, strong x-ray

sources that usually require large devices can be created by smaller and less costly experimental setups.

Hot electrons created during the interaction of subpicosecond, high-intensity lasers with both solid targets and clusters have significant effects on the x-ray radiative properties of the produced plasmas; these effects have been studied extensively in recent years. A two-temperature plasma model with a low-temperature (100–200 eV) Maxwellian electron distribution function (EDF) and hot-electron fractions of 10^{-5} – 10^{-3} at a few keV has been successful in describing K - and L -shell emission spectra from solid Mg, Al, and Cu laser targets [13–15]. A two-temperature model with hot-electron fractions of 10^{-7} – 10^{-5} has been successful in describing K -shell emission spectra from laser-irradiated Ar gas jets [16–20] and plasma focus devices [21]. The most recent studies of Ar clusters irradiated by 35-fs laser pulses have shown that fast laser interaction can produce plasmas with larger hot-electron fractions (10^{-2}) and higher temperatures (400 eV), evidenced by the presence of H-like emission [17]. These studies have demonstrated that hot electrons increase the ionization balance [14,15,21] and augment the intensity of inner-shell satellite lines [13], leaving characteristic signatures on the emission spectra. In this paper, we describe the

effects of hot electrons, time dependence, and opacity on the L -shell spectra of multicharged Kr ions irradiated by fs-laser pulses. In Sec. II, the Kr laser plasma experiments are described, the experimental spectra are shown, and F-, Ne-, and Na-like lines are identified and tabulated with theoretical data. In Sec. III, the collisional-radiative kinetics model is described and the effects of temperature, density, hot-electron fractions, data sources, and opacity on modeled emission spectra and ionization balance curves are given. In Sec. IV, the model of laser interaction with Kr clusters and a time-dependent kinetics analysis are presented. Section V presents the comparisons of the model results to three different experimental spectra. A comparison of our results with previous work is given in Sec. VI and in Sec. VII we provide a summary and discussion of this work.

II. EXPERIMENTS

The experiments were conducted at the laser installation CELIA in Bordeaux, France and at UHI10 in Saclay, France. The CELIA laser source [22,23] produces terawatt-level fs pulses at high repetition rates. A Ti:sapphire oscillator produces 10-fs pulses which are amplified by a series of four amplifiers, using chirped pulse amplification to avoid any damage in the chain. The amplifiers utilize Ti:sapphire crystals as the gain medium and are pumped by five Nd:YLF lasers running at 1 kHz repetition rate. The pulse duration can be adjusted between 20 fs and several picoseconds. A regenerative amplifier introduces a prepulse, which has several nanoseconds duration and appears in front of the main pulse. The contrast ratio between the main and secondary pulses could be varied from 10 to 10^6 . In order to increase the quality of the rising edge of the short pulse, we restricted ourselves to 35–500-fs laser pulse durations and 15 mJ of energy. A 6 micron laser spot radius is obtained in vacuum with an $f/2$ off-axis mirror with a 75-mm focal length. The maximum laser intensity on target with a 35-fs pulse duration is $(1-2) \times 10^{17}$ W/cm².

The UHI10 laser source [24] is a two-beam 10 Hz Ti:Sapphire system with 10 TW peak power on the main beam. The low-energy ultrashort pulse is produced by a modified commercial Ti:sapphire oscillator and is stretched up to 300 ps by an aberrationfree Offner stretcher. After four amplification stages, the pulse energy is about 1.2 J and 600 mJ after recompression. The pulse is recompressed down to 60 fs in a vacuum chamber directly connected to the experimental chamber. A small amount of energy is picked up between the third and fourth amplifier and is then sent to a second compressor. This beam has a 4 mJ energy (after recompression) and the pulse is recompressed in air. The contrast is measured to be about 10^6 for ns time scale and about 10^5 at 1 ps on the main beam with a high-dynamic cross correlator. The corresponding Rayleigh length and vacuum intensity are $600 \mu\text{m}$ and 7×10^{17} W/cm², respectively.

Cluster targets were produced in the vacuum chamber by a pulsed supersonic gas jet. The gas targets at Saclay were formed by a conical nozzle with big input and output holes (1 and 5 mm, respectively), while at Bordeaux a Laval nozzle with medium-sized input and output holes (0.8 and 2.5

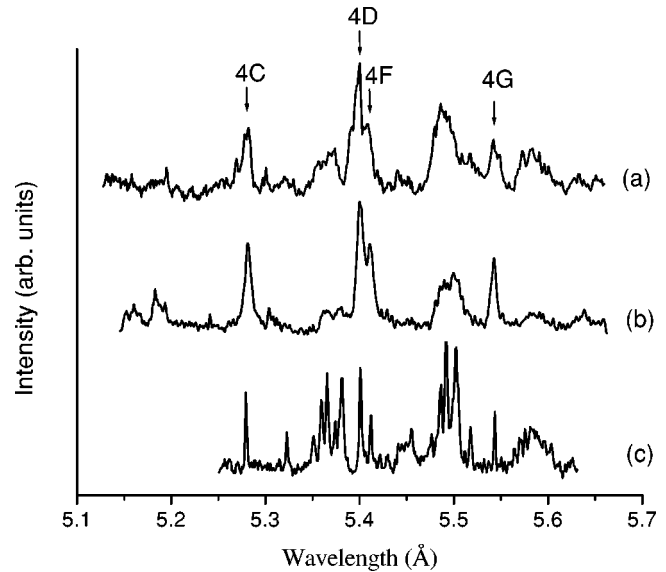


FIG. 1. Experimental Kr laser plasma L -shell spectra: (a) femtosecond-laser plasma from Bordeaux with Laval nozzle, (b) femtosecond-laser plasma from Saclay with conical nozzle (this spectrum was obtained with spatial resolution in the direction of laser propagation and corresponds to the distance 0.66 mm from the beginning of x-ray radiation in plasma), (c) nanosecond-laser plasma [32].

mm, respectively) was used. The experiment at Saclay had a maximum backing pressure of 15 bar and the Bordeaux experiments had about 35 bar. Mathematical modeling [19,25,26] of two-phase gas flow in such nozzles showed that the number of Kr atoms per cluster reached about 2.5×10^7 and 2×10^6 at Saclay and Bordeaux, respectively [27].

The x-ray spectral measurements were conducted using an x-ray focusing spectrometer with spatial resolution (FSSR) [28–31]. A spherically bent mica crystal ($R = 150$ mm) and direct exposure film (DEF) Kodak x-ray film were used for the spectrometer in the Saclay experiments. The spectrometer was oriented in such a way that spatial resolution in the direction of laser propagation was obtained. In the Bordeaux experiments, a spherically bent mica crystal ($R = 100$ mm) and an x-ray charge coupled device camera were used for the spectrometer [23] and spatial resolution in the direction perpendicular to the laser propagation was obtained. For the current investigations into the Bordeaux spectra, the spectral region from 5.0–5.65 Å was recorded. The spectral resolution ($\lambda/\Delta\lambda$) is about 5000 for the Saclay experiments and 4000 for Bordeaux. The spatial resolution is 30–40 μm at Saclay and 80 μm at Bordeaux.

Examples of fs spectra from Bordeaux and Saclay are given in Figs. 1(a) and 1(b), respectively. Figure 1(c) shows a spectrum observed using the same type of FSSR spectrometer from an earlier experiment with Kr clusters irradiated with ns-laser pulses [32]. The contributions of F-like through Mg-like ion emission to the L -shell spectrum are given in the decomposed spectrum of Fig. 2, which was calculated with the model described below. The Ne-like 4–2 lines are labeled with their common designations in Fig. 2. These four distinct Ne-like lines and satellite structures from Na- and

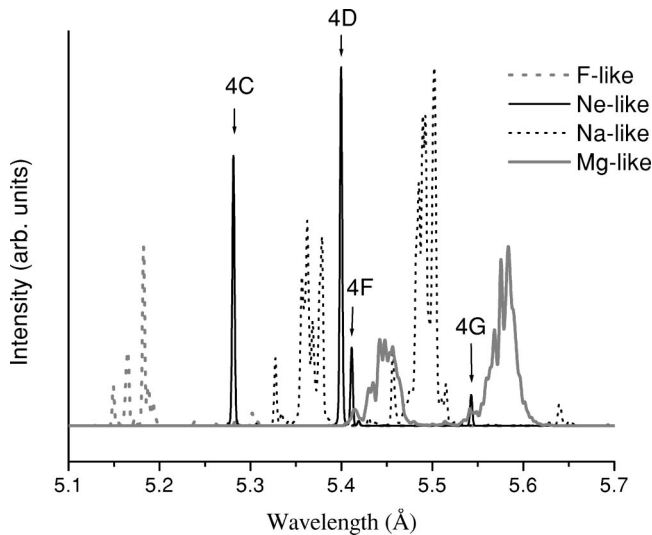


FIG. 2. Modeled spectrum decomposed into contributions from F-like through Mg-like Kr. The contributions from Ne- and Na-like Kr are normalized to 1 and the contributions from F and Mg are normalized to 0.5 so that the features from each ionization stage are clear.

Mg-like Kr are evident in all of the experimental spectra in Fig. 1, while lines from F-like Kr are prominent only in the experimental spectrum from Saclay.

The experimental spectrum from the ns-laser plasma has well-resolved lines and is dominated by Na-like emission, while both fs-laser spectra have much broader lines and are dominated by Ne-like emission. Experimental wavelengths were determined using a relative calibration fixed by the Ne-like 4C line. Experimental relative intensities were determined by normalizing each spectrum to its most intense feature. The narrow Ne- and Na-like lines in the ns spectrum have wavelengths determined to within 1 mÅ and the broader F-like lines in the Saclay fs spectrum have wavelengths determined to within 2.5 mÅ. Experimental wavelengths and relative intensities, theoretical wavelength values, and radiative decay rates for F-, Ne-, and Na-like transitions are given in Table I. The experimental wavelengths of the Ne-like lines are consistent with previous absolute wavelength measurements [33]. The Mg-like satellite structures are composed of so many transitions that line identification is difficult; the structures centered at 5.45 Å and 5.58 Å are both composed largely of transitions from $2s^2 2p^5 3s 3d 4d$ and $2s^2 2p^5 3p 3d 4d$ to $2s^2 2p^6 3l 3l'$.

III. KINETICS MODEL

The time-dependent collisional-radiative kinetics model calculates the populations of all the energy levels relevant to the construction of *L*-shell spectra. The model includes ground states of all ionization stages, from the bare ion to the neutral Kr atom, and fine-structure levels for F-, Ne-, Na-, and Mg-like ions. Details of the configurations considered are given in Table II.

Ionization potentials were taken from published tables [34,35]. The ground states of all ionization stages are linked

by three processes: modified Lotz collisional ionization [36], three-body recombination, and Kramers radiative recombination [37]. Collisional ionization of the valence electron and at least the first inner-shell electron is included for all non-autoionizing states so that, for example, the excited states in Ne-like Kr belonging to $2s^2 2p^5 4s$ are coupled to states belonging to $2s^2 2p^5$, $2s^2 2p^4 4s$, and $2s 2p^5 4s$ in F-like Kr.

The energy level structures and dipole radiative decay rates between all nonautoionizing levels of F-, Na-, Ne-, and Mg-like ions were calculated with Cowan's Hartree-Fock atomic structure code [38]. Auger decay rates from autoionizing levels of the Na- and Mg-like ions and dipole radiative decay rates between the autoionizing levels of Na-like ions were also calculated with Cowan's code. We found that coupling between autoionizing states in the Na-like ions has negligible effects on the Na-like satellite structure and overall ionization balance, so we have not calculated dipole decay rates between autoionizing states of the Mg-like ion. In the special case of Ne-like Kr, selected level energies and electric and magnetic dipole and quadrupole ($E1$, $M1$, $E2$, $M2$) radiative decay rates to the ground state were calculated using second-order many-body perturbation theory with Dirac-Fock potentials [39].

Collision strengths of transitions between excited states were determined by dipole oscillator strengths through the Van-Regemorter approximation [40]. Collision strengths for excitation from low-lying levels of F-, Ne-, and Na-like Kr to excited states were taken or extrapolated from published tables [41–43]. All collision strengths are fit to a general function of the impact electron energy x in threshold units ($\Omega = c_0 + c_1/x + c_2/x^2 + c_3 \ln x$) and integrated over the electron distribution function. The EDF is composed of a Maxwellian portion at the bulk electron temperature T_e and a non-Maxwellian, Gaussian distribution for hot electrons with fraction f . The Gaussian distribution has a width of 200 eV and is centered about the energy T_{hot} , which we take to be 5 keV, as in previous analyses of *K*-shell Ar [14]. At high energies, most collision cross sections are only weakly dependent on the impact electron energy, so the non-Maxwellian portion of collisional rates calculated with this EDF are only weakly dependent on the value of T_{hot} and are practically independent of the width of the Gaussian distribution, unless it is so wide that a significant fraction of hot electrons have energies below the threshold energy for a given transition. In fact, a δ function at T_{hot} is an excellent approximation.

The effect of a Gaussian distribution of hot electrons on a collisional rate is dependent on the bulk temperature of the plasma and the transition energy. Two EDFs with the same fraction of hot electrons in Gaussian tails but different T_e are given in Fig. 3. For a transition with threshold energy small enough to see a significant portion of the Maxwellian electrons, the Gaussian portion of the EDF may contribute only a few percent to its total rate or even decrease the total rate slightly. However, for a transition whose threshold energy is so large that the Maxwellian portion of the EDF is insignificant, the Gaussian portion may account for almost 100% of the total rate. There are two consequences of this. First, a given fraction of hot electrons will have a larger effect at

TABLE I. Line identification for F through Na-like Kr.

Ion	$\lambda_{\text{expt.}}$ (Å)	$\lambda_{\text{theor.}}$ (Å)	Upper level			Lower level		A_r (10^{13} s^{-1})	A_a (10^{13} s^{-1})	Expt. Int.
			Conf.	L_1S_1	LS	Conf.	LS			
F	5.1602 ^a	5.1634 ^b	$2s^2 2p^4 4d$		$2P_{1/2}$	$2s^2 2p^5$	$2P_{1/2}$	44.2 ^b		0.2 ^a
		5.1656 ^b	$2s^2 2p^4 4d$		$2D_{3/2}$	$2s^2 2p^5$	$2P_{1/2}$	28.2 ^b		
F	5.1827 ^a	5.1822 ^b	$2s^2 2p^4 4d$		$2D_{5/2}$	$2s^2 2p^5$	$2P_{3/2}$	28.9 ^b		0.3 ^a
		5.1829 ^b	$2s^2 2p^4 4d$		$2D_{3/2}$	$2s^2 2p^5$	$2P_{3/2}$	18.3 ^b		
F	5.1934 ^a	5.1886 ^b	$2s^2 2p^4 4d$		$2P_{1/2}$	$2s^2 2p^5$	$2P_{3/2}$	13.4 ^b		0.2 ^a
		5.1927 ^b	$2s^2 2p^4 4d$		$2P_{3/2}$	$2s^2 2p^5$	$2P_{1/2}$	12.4 ^b		
F	5.3036 ^a	5.3018 ^b	$2s^2 2p^4 4s$		$2P_{3/2}$	$2s^2 2p^5$	$2P_{3/2}$	2.95 ^b		0.16 ^a
Ne	5.2780 ^c	5.2812 ^d	$2s^2 2p^5 4d$		$1P_1$	$2s^2 2p^6$	$1S_0$	24.0 ^d		0.6 ^c
4C		5.2786 ^e						27.0 ^e		
Ne	5.3995 ^c	5.3995 ^d	$2s^2 2p^5 4d$		$3D_1$	$2s^2 2p^6$	$1S_0$	29.7 ^d		0.8 ^c
4D		5.3968 ^e						33.0 ^e		
Ne	5.4114 ^c	5.4112 ^d	$2s^2 2p^5 4s$		$1P_1$	$2s^2 2p^6$	$1S_0$	6.13 ^d		0.42 ^c
4F		5.4089 ^e	$2s^2 2p^5 4s$		$1P_1$	$2s^2 2p^6$	$1S_0$	5.10 ^e		
Ne	5.5424 ^c	5.5426 ^d	$2s^2 2p^5 4s$		$3P_1$	$2s^2 2p^6$	$1S_0$	1.71 ^d		0.45 ^c
4G		5.5405 ^e						1.80 ^e		
Na	5.3217 ^c	5.3274 ^b	$2s^2 2p^5 3p4d$	($1S$)	$2D_{3/2}$	$2s^2 2p^6 3p$	$2P_{1/2}$	7.32 ^b		0.29 ^c
Na	5.3500 ^c	5.3523 ^b	$2s^2 2p^5 3d4d$	($1P$)	$2D_{3/2}$	$2s^2 2p^6 3d$	$2D_{3/2}$	11.1 ^b	25.9 ^b	0.27 ^c
Na	5.3581 ^c	5.3561 ^b	$2s^2 2p^5 3p4d$	($1S$)	$2D_{5/2}$	$2s^2 2p^6 3p$	$2P_{3/2}$	2.74 ^b	0.37 ^b	0.55 ^c
Na	5.3643 ^c	5.3624 ^b	$2s^2 2p^5 3p4d$	($3P$)	$2D_{5/2}$	$2s^2 2p^6 3p$	$2P_{3/2}$	19.7 ^b	9.34 ^b	0.76 ^c
Na	5.3733 ^c	5.3683 ^b	$2s^2 2p^5 3p4d$	($3D$)	$4F_{3/2}$	$2s^2 2p^6 3p$	$2P_{1/2}$	14.5 ^b	11.1 ^b	0.38 ^c
Na	5.3805 ^c	5.3789 ^b	$2s^2 2p^5 3d4d$	($1D$)	$2D_{5/2}$	$2s^2 2p^6 3d$	$2D_{5/2}$	12.4 ^b	16.3 ^b	0.72 ^c
Na	5.4546 ^c	5.4564 ^b	$2s^2 2p^5 3p4d$	($1S$)	$2D_{5/2}$	$2s^2 2p^6 3p$	$2P_{3/2}$	6.2 ^b	30.8 ^b	0.31 ^c
Na	5.4752 ^c	5.4746 ^b	$2s^2 2p^5 3d4d$	($1P$)	$2D_{5/2}$	$2s^2 2p^6 3d$	$2D_{5/2}$	9.01 ^b	17.1 ^b	0.28 ^c
		5.4769 ^b	$2s^2 2p^5 3p4d$	($1P$)	$2P_{1/2}$	$2s^2 2p^6 3p$	$2P_{1/2}$	2.55 ^b	50.6 ^b	
Na	5.4865 ^c	5.4858 ^b	$2s^2 2p^5 3p4d$	($3P$)	$2D_{5/2}$	$2s^2 2p^6 3p$	$2P_{3/2}$	11.0 ^b	33.7 ^b	0.67 ^c
Na	5.4921 ^c	5.4892 ^b	$2s^2 2p^5 3p4d$	($1D$)	$2D_{3/2}$	$2s^2 2p^6 3p$	$2P_{1/2}$	31.6 ^b	0.15 ^b	1.0 ^c
		5.4923 ^b	$2s^2 2p^5 3d4d$	($3D$)	$2F_{7/2}$	$2s^2 2p^6 3d$	$2D_{5/2}$	20.3 ^b	24.7 ^b	
Na	5.5025 ^c	5.5017 ^b	$2s^2 2p^5 3p4s$	($3D$)	$4D_{3/2}$	$2s^2 2p^6 3p$	$2P_{1/2}$	2.43 ^b	9.20 ^b	0.96 ^c
Na	5.5176 ^c	5.5145 ^b	$2s^2 2p^5 3d4d$	($3F$)	$2D_{5/2}$	$2s^2 2p^6 3d$	$2D_{5/2}$	4.11 ^b	2.08 ^b	0.33 ^c

^aExperimental data from the present work (the Saclay fs spectrum).^bTheoretical data using the COWAN code.^cExperimental data from Ref. [32] (the ns laser plasma spectrum).^dTheoretical data using the RMBPT code.^eTheoretical data using the HULLAC code.

TABLE II. Levels included in the kinetics model.

Ion	Levels	Configurations	Autoion. Conf.
F	249	$2s^2 2p^5, 2s2p^6, 2s^2 2p^4 nl,$ $2s 2p^5 nl; n=3, 4$	
Ne	157	$2s^2 2p^6, 2s^2 2p^5 nl,$ $2s 2p^6 nl; n=3-5$	
Na	995	$2s^2 2p^6 nl; n=3, 4$	$2s^2 2p^4 n ln'l',$ $2s 2p^5 n ln'l'; n, n'=3, 4$
Mg	914	$2s^2 2p^6 nl nl'; n=3$	$2s^2 2p^5 3l 3l' nl'',$ $2s^2 2p^6 3l 3l' nl''; n=3, 4$

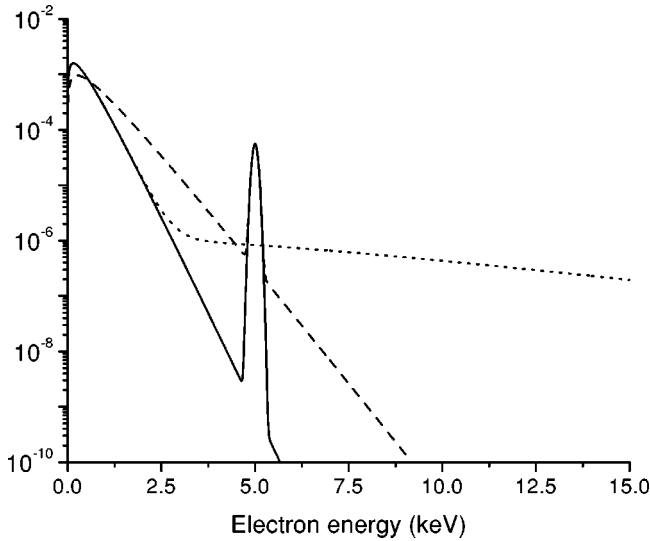


FIG. 3. Electron distribution functions: the solid and dashed lines are composed of a Maxwellian portion with $T_e = 200$ eV and 500 eV, respectively, and Gaussian distribution for hot electrons with fraction $f = 10^{-2}$ centered at 5 keV. The dotted line includes a Maxwellian portion with $T_e = 200$ eV and a Maxwellian distribution for hot electrons with $f = 10^{-2}$ and $T_{\text{hot}} = 5$ keV.

smaller T_e so that higher temperatures require larger portions of hot electrons in order for their effects to become pronounced. Second, deexcitation rates, which have a threshold energy of zero, are practically unaffected by the presence of a small fraction of hot electrons. Therefore, collisional deexcitation and recombination rates in this work are found by detailed balance using only the Maxwellian portions of corresponding excitation rates.

The magnitude of the effect of hot electrons on a transition rate is also dependent on the broad functional form of the electron distribution. Hot electrons represented by a second Maxwellian distribution at T_{hot} will in general contribute at least one order of magnitude more than a Gaussian tail. The reason for this is illustrated in Fig. 3, which shows various electron distribution functions. The second Maxwellian persists to high energies so it has a significant effect on transitions with large threshold energies, just like the Gaussian tail, but the Maxwellian is spread out, ensuring that it affects all transitions near their threshold values, where their collision cross sections are generally largest. We include this EDF for comparison to the *L*-shell model of Cu [15].

The time-dependent population of a level i is given by

$$\frac{dX_i}{dt} = \sum_{j=1}^N X_j W_{ji} - X_i \sum_{j=1}^N W_{ij}, \quad (1)$$

where W_{ij} is the sum of spontaneous and collisional rates that transfer population from level i to level j . Time-dependent level populations are found by setting appropriate initial conditions and numerical integration of the coupled rate equations. At steady state, dX/dt is zero and equilibrium level populations are found using standard matrix methods.

The line intensity of a transition between levels i and j with radiative decay rate $A_r(ij)$ is given by I_{ij}

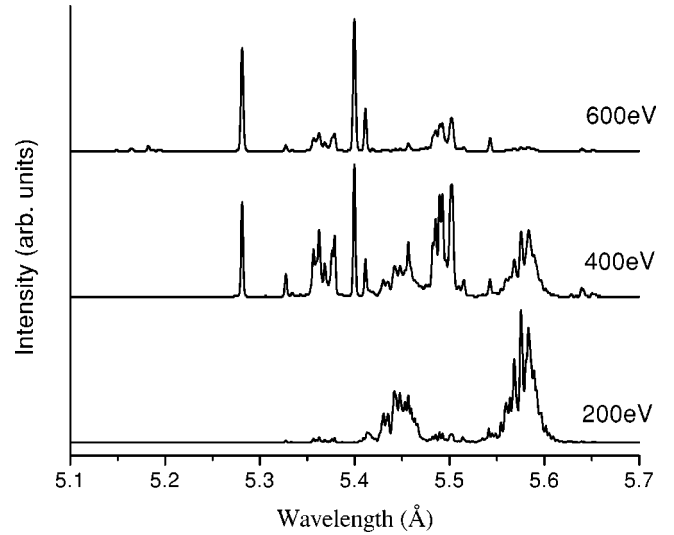


FIG. 4. Modeled spectra with electron density $n_e = 10^{21} \text{ cm}^{-3}$, no hot electrons, no opacity, and various electron temperatures.

$= X_j A_r(ij) \hbar \omega_{ij}$. Each line is given a Voigt line profile with Doppler broadening determined by the ion temperature (taken to be equal to the electron temperature) and Lorentz broadening determined by the sum of spontaneous and collisional rates of depopulation for both the upper and lower levels. Both types of broadening are multiplied by separate factors that can be artificially varied to account for instrument resolution and other effects that are not explicitly modeled. The physical processes that give rise to line broadening in the fs plasma spectra would make an interesting subject for future study.

A. Model results

This section presents the variation of the modeled spectra with changes in the electron density, EDF, and plasma size. The dependence of modeled spectra on electron temperature is given in Fig. 4. The ionization balance increases with the electron temperature so that higher ionization stages dominate the spectra, but there is little change in the relative intensities of lines within a single ionization stage. The electron density dependence of modeled spectra is shown in Fig. 5. Increasing density increases the ionization balance significantly and also changes the shape of the Na- and Mg-like satellite structures and the relative intensities of Ne-like lines. In particular, increasing density tends to amplify the long-wavelength satellites within a group. The dependence of modeled spectra on the fraction of hot electrons f is given in Fig. 6. Increasing the fraction of hot electrons changes both the ionization balance and the shape of the satellite structures and tends to amplify short-wavelength satellite lines. In contrast to studies of *K*-shell Ar emission [16], hot-electron fractions less than 10^{-3} do not have significant effects on the Kr *L*-shell spectra. This is because at low temperatures (< 200 eV), the Kr plasma is ionized only up to the Si-like ionization stage. Emission from ionization stages beyond Mg are not modeled here, so the effects of hot-electrons on the modeled emission spectra are not apparent until the hot electron fraction is sufficient to affect at least

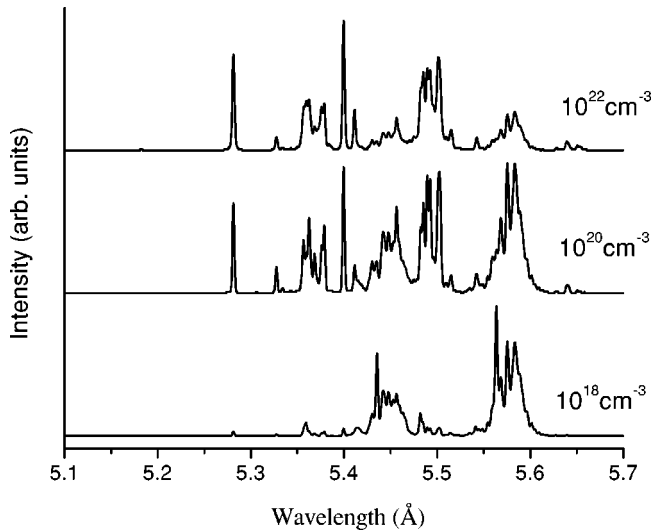


FIG. 5. Modeled spectra with electron temperature $T_e = 400$ eV, no hot electrons, no opacity, and various electron densities.

the Mg-like charge state. At $f \approx 10^{-2}$, the effects of hot electrons are pronounced and Ne-like lines dominate the spectra.

To facilitate an understanding of the effects of hot electrons on the ionization stages, we present ionization balance curves as a function of both electron temperature and hot-electron fraction in Figs. 7 and 8, respectively. A hot-electron fraction of about 2% at 200 eV (Fig. 8) gives approximately the same ratio of Na- to Ne- and Mg-like ions as that of an electron temperature of 350 eV with no hot electrons (Fig. 7), but the F-like ion population is an order of magnitude larger in the case with hot electrons. Thus, hot electrons affect L -shell spectra in two characteristic ways: they spread out the ionization balance so that significant populations of widely separated ions can exist together, and they alter satellite structures.

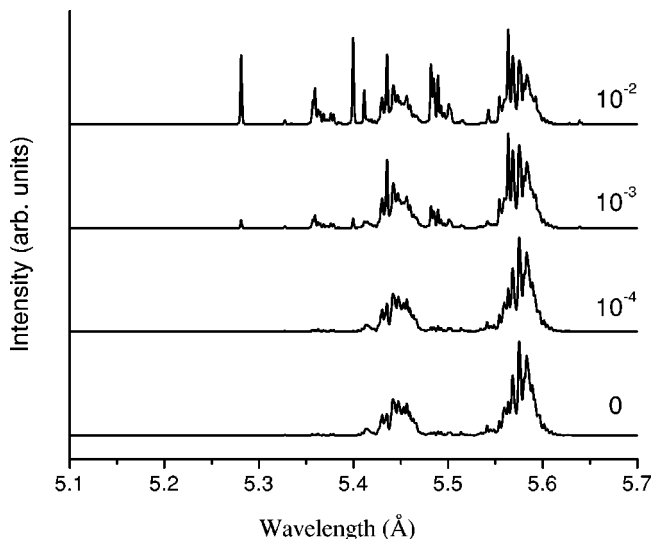


FIG. 6. Modeled spectra with electron temperature $T_e = 200$ eV, electron density $n_e = 10^{20} \text{ cm}^{-3}$, no opacity, and various fractions of hot electrons.

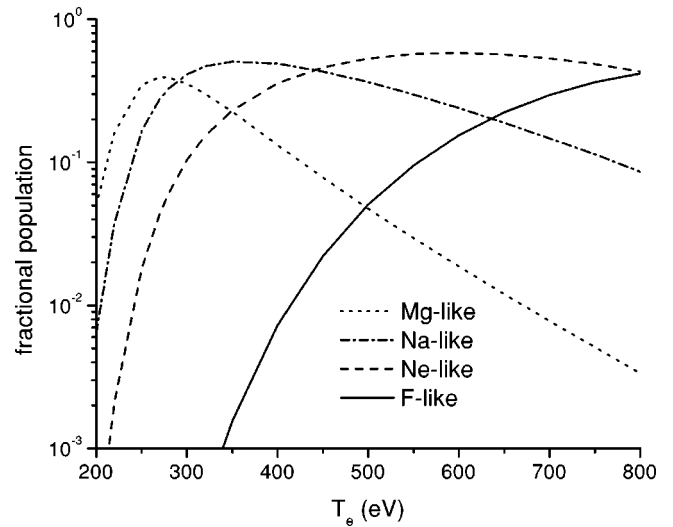


FIG. 7. Modeled ionization stage populations vs electron temperature for $n_e = 2 \times 10^{21} \text{ cm}^{-3}$ and $f = 0$.

B. Variation of atomic data

Although variations in the electron density and the fraction of hot electrons affect the structure of satellite features, neither parameter has a large effect on the relative intensity of the Ne-like $4G$ line. A casual comparison of the experimental and modeled spectra so far presented immediately reveals discrepancies in this spectral feature. The $4G/4D$ ratio is around 0.5 in all of the experiments, but all modeled spectra given so far have $4G/4D$ ratios around 0.1–0.2. The insensitivity of the $4G/4D$ ratio to plasma parameters stands in marked contrast to the $3G/3D$ ratio, which is quite sensitive to variations in the electron density and has been previously used as a density diagnostic [44–47]. The $3F$ and $3G$ lines are emitted from a clump of the lowest-energy excited levels in the Ne-like ion and their populations are sensitive to density-dependent radiative cascades from levels with higher energies. The $4F$ and $4G$ lines are not as sensitive to cas-

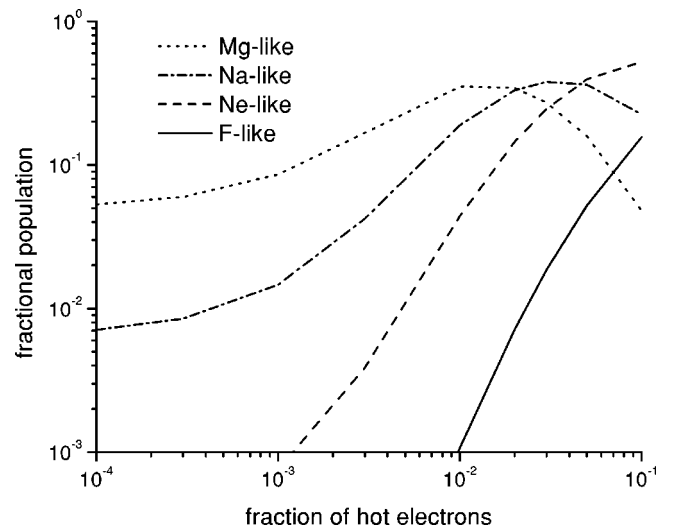


FIG. 8. Modeled ionization stage populations vs hot-electron fraction for $n_e = 2 \times 10^{21} \text{ cm}^{-3}$ and $T_e = 500$ eV.

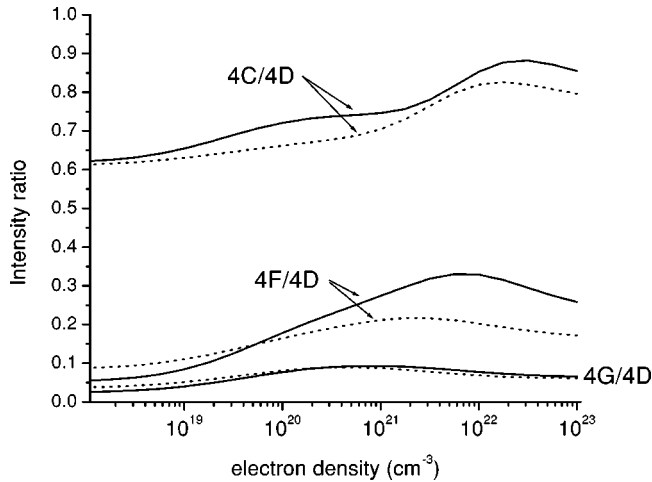


FIG. 9. Ratios of $4X/4D$ lines as a function of density at $T_e = 500$ eV (no hot electrons and no opacity) for two different Ne-like data sets. The solid line gives intensity ratios obtained using a compiled data set Refs. [36,37,40] and dipole radiative Van-Regemorter collisional coupling between excited Ne-like levels. The dashed line gives intensity ratios obtained using HULLAC data (Ref. [46]) with full radiative and collisional coupling between excited Ne-like levels.

acades and so are not useful as density diagnostics, which is unfortunate. But if the small relative intensity of the $4G$ line in the modeled spectra is not due to an inaccuracy of the model, a parameter other than the ones so far considered must be introduced in order to obtain agreement with the experiment.

To ensure that the difficulty in describing the $4G$ Ne-like line of the laser plasma spectra is not due to gross inaccuracies of atomic data or inadequacies of coupling in the kinetics model, we have consulted a completely different data source for the Ne-like ion. A complete set of HULLAC data [48,49] including $E1$, $E2$, $M1$, and $M2$ radiative rates and collision strengths for excitation between all Ne-like levels was substituted for the compiled Ne-like data scheme described above. The HULLAC dipole radiative decay rates, the data with the most direct influence on line intensities, are given in Table I for comparison with the RMBPT calculations [39]. The agreement between the data sources for these rates is fair, with 5–15% discrepancies in absolute values, and is sufficient to exclude inaccuracy of the dipole decay rates as the source for disagreement between modeled and experimental Ne-like line intensities. However, the Ne-like levels are coupled by only dipole radiative and approximated dipole collisional rates in the compiled data scheme, and it is possible that either the incompleteness of this coupling or the inadequacy of the Van Regemorter approximation could be responsible for the disagreement between model and experiment. The HULLAC data set, in contrast, includes complete radiative and collisional coupling of Ne-like levels.

A comparison of Ne-like line ratios computed with the kinetics model using the HULLAC and compiled data sets is given in Fig. 9. The figure shows good agreement between the two data schemes for the $4G/4D$ ratio, which is our primary concern. The agreement between the two is worst

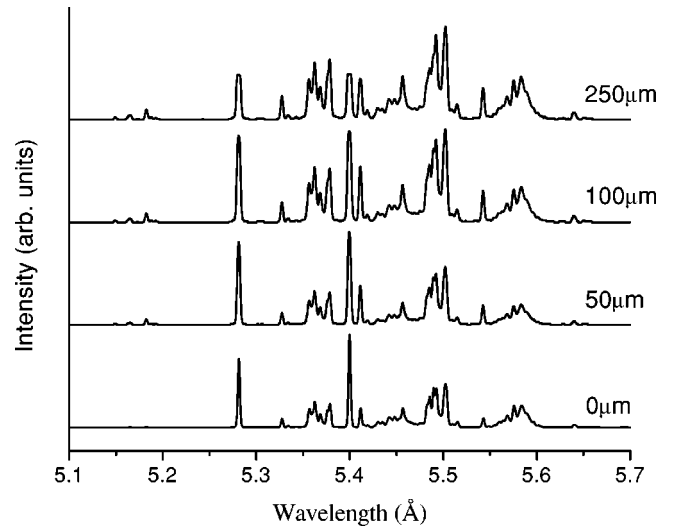


FIG. 10. Modeled spectra with electron temperature $T_e = 500$ eV, electron density $n_e = 10^{20}$ cm^{-3} , no hot electrons, and various plasma diameters.

for the $4F/4D$ lines ratio, but that disagreement may be largely due to the large 25% discrepancy in the ratios of the $4F/4D$ radiative decay rates between the data sources. The $4C/4D$ ratio is a more informative case because both data sources agree to within 1% on this ratio of dipole decay rates. Thus, the impact of different coupling schemes and rates of secondary influence are isolated and the magnitude of their effects can be estimated. The fair agreement of the $4C/4D$ intensity ratios between the data schemes indicates that the kinetics model using the compiled data scheme is sufficiently accurate and that we must look elsewhere to resolve the discrepancies in Ne-like line intensities between the modeled and experimental spectra. The compiled data scheme is used for all modeled spectra in this paper.

C. Opacity

The relatively large oscillator strengths of the Ne-like $4C$ and $4D$ lines suggest that they may be more susceptible to absorption than the $4G$ and $4F$ lines. Opacity effects are therefore a promising avenue for the resolution of the discrepancies of the relative intensities of these lines between experimental and modeled spectra. Opacity is included with a simple absorption model [50] that treats the plasma as a homogeneous slab. The opacity of a line in this model is dependent on the density of ions in the lower level of a transition and the oscillator strength of the transition, and since the lower level is the Ne-like ground state for all the $4X$ transitions, opacity effects increase the $4G/4D$ and $4F/4D$ Ne-like line ratios dramatically. Including opacity also increases the relative intensity of lines from other ionization stages, which tend to have both smaller oscillator strengths and less populated lower levels. These effects are illustrated in Fig. 10, which shows modeled spectra at 500 eV and 10^{20} cm^{-3} with various plasma diameters.

The impact of opacity is dependent on the electron density as well as the plasma size, since line absorption is dependent on the density of ions, which is proportional to the

electron density in a neutral plasma. The magnitude of opacity effects for a plasma with a $100\ \mu\text{m}$ diameter at $10^{20}\ \text{cm}^{-3}$ are comparable to the magnitude of opacity effects for a plasma with a $10\ \mu\text{m}$ diameter and an electron density of $10^{21}\ \text{cm}^{-3}$. The emitting regions of both the ns and fs-laser plasmas have a measured size of about $200\ \mu\text{m}$. The clusters in the ns plasma have enough time to expand to form a relatively homogeneous plasma with an electron density near $10^{20}\ \text{cm}^{-3}$ for which our opacity model is well suited. In contrast, the dense ($n_e > 10^{21}\ \text{cm}^{-3}$) clusters in the fs-laser plasma persist during emission. The clusters have diameters around $0.06\text{--}0.07\ \mu\text{m}$ and the distance between clusters is around $1.5\ \mu\text{m}$ [27], so along a line of sight the effective absorbing size of the fs plasma is around $8\ \mu\text{m}$. This line of reasoning implies that the opacity effects on both the ns and fs-laser plasma spectra are of comparable magnitude. However, treating the clusters as a small homogeneous lump neglects the structure and inhomogeneity of the fs-laser plasma.

This opacity model is adequate for a general description of absorption effects, but it is not self-consistent; that is, the absorbed radiation has no effect on the population kinetics. However, previous work [51] shows similar results for opacity effects on high- n Ne-like Cu lines with a self-consistent model of opacity. Including absorption in the kinetic equations increases the ionization balance and has an effect similar to that of increasing the electron temperature. Therefore, the results presented here with opacity may have temperatures slightly higher than would be obtained with a self-consistent model of absorption.

IV. PLASMA MODEL

The experimental laser pulse contrast was $10^4\text{--}10^5$ in a $1\text{--}2\text{-ps}$ time scale, so that the laser flux density reached values of $10^{12}\text{--}10^{14}\ \text{W/cm}^2$ before the main pulse. This flux density is large enough to partially destroy the clusters and to create electron temperatures of $T_{\text{cold}} = 100\text{--}200\ \text{eV}$ in the expanding clusters and the surrounding bulk plasma. The pre-formed plasma is spatially inhomogeneous and has enough time to reach near-steady-state conditions, with P-like to Mg-like Kr ions existing in both the clusters and the surrounding bulk plasma. In the next stage, the main fs-laser pulse interacts with the nonuniform preheated plasma. The pulse energy is strongly absorbed in the parts of the clusters which have densities above the critical density associated with the laser frequency ($n_{\text{crit}} \approx 1.7 \times 10^{21}\ \text{cm}^{-3}$).

Thus, in a small volume with some characteristic dimension r_{hot} , the main pulse creates a lot of hot electrons with energies on the order of $T_{\text{hot}} \approx 3\text{--}10\ \text{keV}$. The dimension r_{hot} may be taken to be approximately the size of the clusters: $0.06\text{--}0.07\ \mu\text{m}$ for both the Laval and conical nozzles. The distance between clusters ($r_{\text{cold}} \approx 1.5\ \mu\text{m}$) [27] can be used as the characteristic dimension of the cooler and less dense bulk plasma. The thermalization time for the hot electrons in the bulk plasma is several tens of picoseconds and their mean free path is several hundred μm . Thus, for some time after the main pulse, the electron temperature in the bulk plasma remains at T_{cold} and there exists some fraction of hot

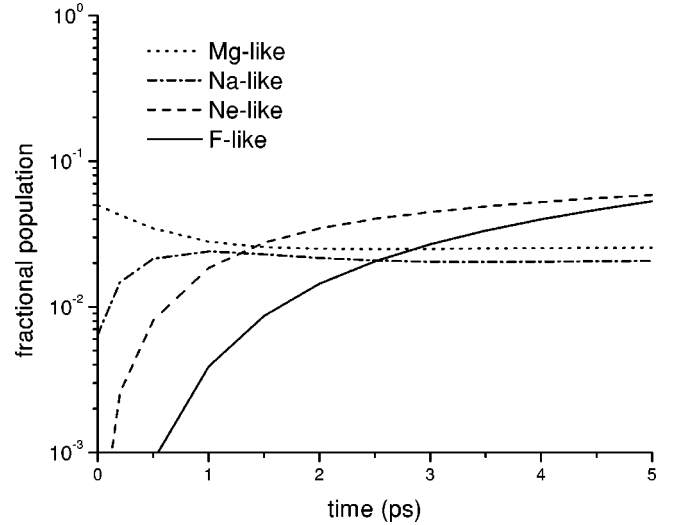


FIG. 11. Modeled ionization stage populations vs time. Initial conditions are steady-state populations at $n_e = 2 \times 10^{21}\ \text{cm}^{-3}$, $T_e = 200\ \text{eV}$, and $f = 0$. At time=0, the main laser pulse interaction with the dense clusters produces $f = 90\%$ hot electrons.

electrons on the order of $(r_{\text{hot}}/r_{\text{cold}})^3 \approx 10^{-4}$ with energy T_{hot} dispersed throughout the plasma.

In the case of K -shell Ar emission from 60-fs laser plasmas, it was adequate to treat the clusters after the main pulse as dense, high-temperature plasma regions with $T_e = T_{\text{hot}}$ with an ionization balance corresponding to steady-state conditions at T_{cold} [16]. In the case of L -shell Kr, this model for the clusters after the main pulse will not produce anything like the experimental spectra, which are dominated by Ne-like lines, since the Ne-like ionization stage has only a small population at T_{cold} . But a time-dependent analysis shows that the ionization balance after the main pulse is not stationary over a ps time scale. Figure 11 gives fractional populations of the emitting ions as a function of time. The initial level populations are those of a steady-state plasma with electron density $n_e = 3 \times 10^{21}\ \text{cm}^{-3}$ and $T_{\text{cold}} = 200\ \text{eV}$. At time=0, the bulk temperature remains the same, but a large fraction of hot electrons is introduced. (We take this fraction to be 90% to correspond with the assumptions of the K -shell Ar model.) After the hot electrons are introduced, the collisional rates are recalculated and the rate equations are numerically propagated over 5 ps. The population moves quickly through the Mg- and Na-like ionization stages and, within a few ps, is concentrated in the F- and Ne-like stages.

A running integral over time of the level populations is used to produce the modeled time-dependent emission spectra in Fig. 12. In these spectra, the lines are artificially broadened so that they resemble the lines in the fs spectrum. A comparison of the time-dependent spectra in Fig. 12 with the experimental spectra in Fig. 1 shows several promising features. The $4C$ line is less intense than it is in the steady-state cases and conforms better to the fs plasma spectra, and the Mg-like feature at $5.45\ \text{\AA}$ has a shape that conforms to the experiment much better than any steady-state case. However, the Ne-like $4F$ and $4G$ lines are much weaker in the time-dependent modeled spectra than in the experimental spectra

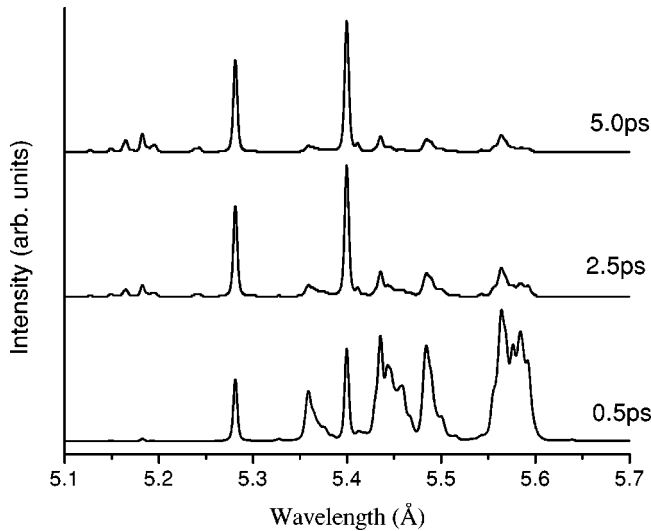


FIG. 12. Modeled spectra calculated from integrated populations at different times after the main laser pulse. Initial conditions are steady-state populations at $n_e=2 \times 10^{21} \text{ cm}^{-3}$, $T_e=200 \text{ eV}$, and $f=0$. At time=0, the main laser pulse interaction with the dense clusters produces $f=90\%$ hot electrons.

and the ratio of Na-like to Mg-like satellite features is too small within 2.5 ps. These discrepancies might be resolved by a better understanding of the evolution of the electron distribution function or of opacity effects in the inhomogeneous plasma. But these considerations are beyond the scope of this work, and the time-dependent analysis is henceforward used only as evidence that the ionization balance after the main pulse is not well described by stationary preplasma conditions. Therefore, we will use a steady-state model to describe the time-averaged cluster emission and vary the temperature and fraction of hot electrons to determine the best fit.

V. COMPARISON WITH EXPERIMENT

The experimental ns spectrum from Fig. 1 is repeated in Fig. 13(a) for comparison between experiment and theory. The best-fitting modeled spectra to the ns-laser plasma spectrum are given in Figs. 13(b) and 13(c). The ns-laser plasma is expected to have an electron temperature between 500–600 eV, an electron density around 10^{20} cm^{-3} , and a plasma size of about 200 μm . The modeled spectrum without opacity, shown in Fig. 13(b), has a temperature chosen to best fit the relative line intensities of different charge states and a density chosen to best fit the shape of the satellite structures. There are, however, several problems with the fit. The Ne-like lines are too intense relative to the Na- and Mg-like satellites. This cannot be mitigated by lowering the temperature, because then the Mg-like lines would be too intense relative to the Na-like lines. Also, the Ne-like 4*G* and 4*F* lines are much smaller than in the experiment and again, this cannot be resolved by changing the electron temperature, density, or the fraction of hot electrons. Finally, the temperature is a bit lower than expected and the density is too high for the experimental conditions. All these difficulties are re-

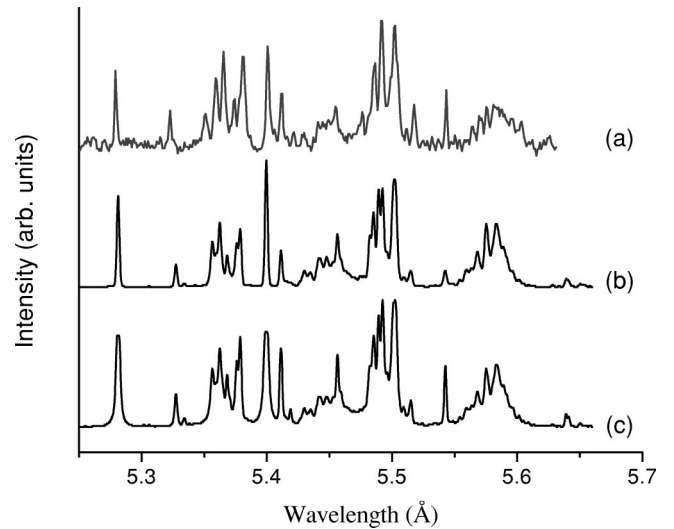


FIG. 13. Comparison of experimental ns spectrum (a) and modeled spectra with and without opacity. The modeled spectrum in (b) has $T_e=400 \text{ eV}$, $n_e=1 \times 10^{21} \text{ cm}^{-3}$, $f=0$, and no opacity effects. The modeled spectrum in (c) has $T_e=600 \text{ eV}$, $n_e=8 \times 10^{19} \text{ cm}^{-3}$, $f=0$, and a plasma size of 200 μm .

solved by including opacity, as shown in Fig. 13(c). The large oscillator strengths of the 4*C* and 4*D* lines make them more susceptible to self-absorption than most other lines in the spectrum, so that the final fit with opacity has good agreement with the experimental spectra in ratios of lines from different charge states and within charge states. Including opacity also entails an increase in temperature and decrease in density so that the final values conform well to the experimental expectations. No better fit to the ns spectrum can be obtained by including hot electrons.

As discussed above, only opacity and time dependence have a major effect on the relative intensities of lines in the Ne-like charge state. Opacity is successful in the description of the spectrum from a uniform, near-steady-state ns-laser plasma. However, the inhomogeneity of the fs-laser-produced plasmas makes the incorporation of our simple slab absorption model problematic, and our knowledge of the EDF evolution in the clusters is insufficient to guide the development of an accurate time-dependent scenario. Therefore, the two effects which might improve the fit of the Ne-like lines in the fs spectra are neglected in the modeling and we attempt simply to find good fits for the relative intensities of different ionization stages and the satellite line structures. For the fs spectra, we assume that $T_{\text{cold}}=200 \text{ eV}$, that the bulk plasma electron density is 10^{20} cm^{-3} and the electron density of the clusters is slightly above n_{crit} ; we take it to be $2 \times 10^{21} \text{ cm}^{-3}$. We assume that the duration of the preplasma is a few ps and approximately equal to the emission duration of the plasma after the laser pulse. The bulk plasma after the main pulse retains the temperature and density of the bulk preplasma, but has a fraction of hot electrons $(r_{\text{hot}}/r_{\text{cold}})^3 = f = 10^{-4}$. This small hot-electron fraction slightly increases the absolute intensity of the emission from the bulk plasma but has little impact on the Mg-like line structure or the ionization balance (see Fig. 6). We assume that the clus-

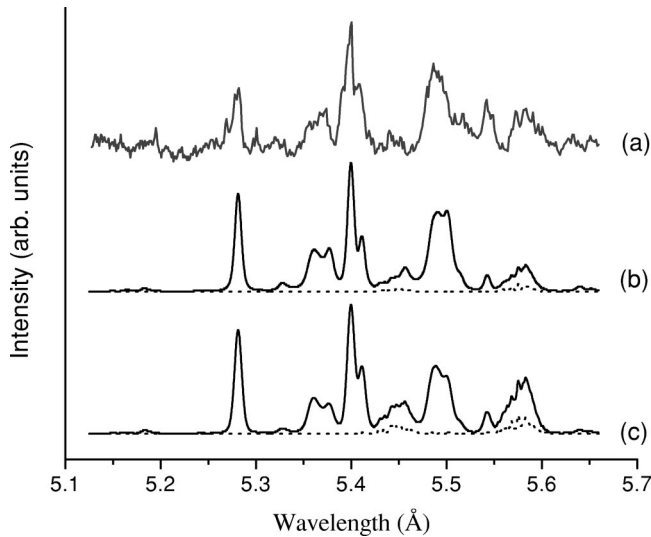


FIG. 14. Comparison of experimental fs spectrum from Bordeaux (a) and modeled spectra with and without hot electrons. The modeled spectrum in (b) has $T_e = 525$ eV, $n_e = 2 \times 10^{21}$ cm $^{-3}$, and $f = 0$. The modeled spectrum in (c) has $T_e = 300$ eV, $n_e = 1 \times 10^{21}$ cm $^{-3}$, and $f = 2 \times 10^{-2}$. The dashed lines show the contribution of the bulk and prepulse plasma regions, which are included in the modeled spectra given by the solid lines in (b) and (c).

ter density after the main pulse remains at 2×10^{21} cm $^{-3}$. The electron temperature and fraction of hot electrons in the clusters after the main pulse were varied to find the best fit to the experimental spectra. The emission from the dense clusters after the main pulse is an order of magnitude larger than the combined emissions from the preplasma and the bulk plasma after the main pulse, even though the emitting volume of the bulk plasma is much larger. Thus, the conditions of three of the four plasma stages have only a small influence on the spectra and are not treated in depth. Comparisons of modeled spectra to the Bordeaux (Laval nozzle) and Saclay (conical nozzle) fs-laser plasma emission spectra are given in Figs. 14 and 15, respectively. The experimental spectra from Fig. 1 are repeated in these figures for comparison, and the best fits with and without hot electrons are shown. The best fits include emission contributions from the preplasma and bulk plasma combined, given by dotted lines in the figures. The preplasma and bulk plasma have a smaller effect on the spectra for higher cluster temperatures, since the absolute intensity of cluster emission increases with temperature.

The best fit for the Bordeaux spectrum (Laval nozzle) without hot electrons has an electron temperature of 525 eV and is shown in Fig. 14(b). The modeled ratios of Na-like to Ne-like lines are in good agreement with experiment. The relatively narrow lines composing the experimental Mg-like structures evidence plasma inhomogeneity. Emission from cool regions of the inhomogeneous plasma contributes narrow Mg-like lines that bring the modeled spectra into better agreement with the experimental spectrum. This emission has been included in both modeled spectra and its relative magnitude is indicated by the dotted lines in Fig. 14(b). However, even with this contribution the spectrum without hot electrons has too little Mg-like emission. We have shown

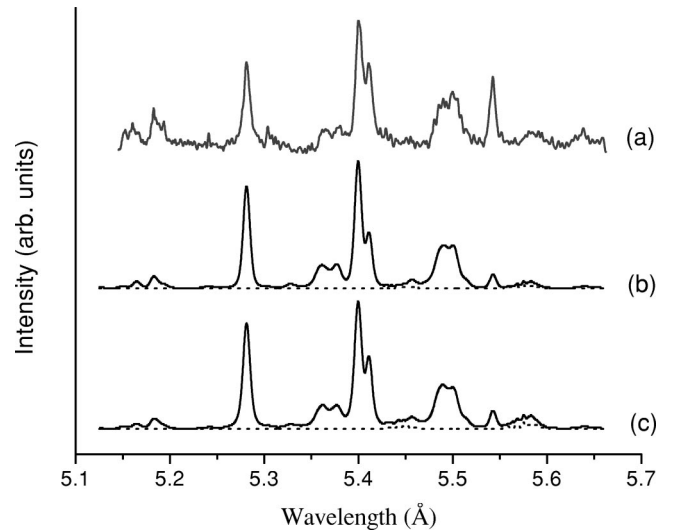


FIG. 15. Comparison of experimental fs spectrum from Saclay (a) and modeled spectra with and without hot electrons. The modeled spectrum in (b) has $T_e = 650$ eV, $n_e = 2 \times 10^{21}$ cm $^{-3}$, and $f = 0$. The modeled spectrum in (c) has $T_e = 400$ eV, $n_e = 2 \times 10^{21}$ cm $^{-3}$, and $f = 4 \times 10^{-2}$. The dashed lines show the contribution of the bulk and prepulse plasma regions, which are included in the modeled spectra given by the solid lines in (b) and (c).

that hot electrons are useful for spreading out the ionization balance so that larger fractions of Mg-like ions can coexist with the same emission ratios of Na-like to Ne-like Kr. This is shown in Fig. 14(c). The synthetic spectrum with hot electrons is a better fit to experiment in another important feature as well. In the single-temperature spectrum, the Na-like satellite structure at 5.49 Å slopes slightly from long wavelengths to shorter wavelengths, while the slope of that structure in the experimental spectrum is reversed. This is precisely the effect of hot electrons, especially large fractions at small electron temperatures (see Fig. 6). The best fit with hot electrons gives good agreement with experiment for both the shape of the Na-like satellite structure and the relative intensities of the Mg- and Na-like features.

The experimental fs spectrum from Saclay (conical nozzle), shown in Fig. 15(a), does not exhibit the reversed slope in the Na-like satellite structure. This does not preclude the existence of hot electrons, because for higher temperatures and larger hot-electron fractions the effect of hot electrons on the shape of the satellite structure is washed out. The evidence for hot electrons in this experimental spectrum is the presence of both Mg- and F-like lines with significant intensity. This indicates a spreading out of the ionization balance characteristic of hot electrons. The best fit to the Saclay spectrum without hot electrons, given in Fig. 15(b), has an electron temperature of 650 eV and has ratios of Na-like to Ne-like lines that are in good agreement with experiment, but both Mg- and F-like features are too weak in the high-temperature spectrum. The high temperature implies a large absolute intensity so that the contribution of Mg-like emission from the preplasma and the bulk plasma does not significantly improve the fit. The best fit with hot electrons, given in Fig. 15(c), has an electron temperature of 400 eV and 4% hot electrons. It has approximately the same ratios of

F- and Na-like line intensities as the spectrum without hot electrons and a better fit to the experimental spectrum of the Mg-like satellites. The improved fit for the Mg-like feature is due in equal parts to the addition of Mg-like emission from the preplasma and bulk plasma, which makes a greater contribution because the absolute intensity of the spectrum with hot electrons is about half that of the spectrum at 650 eV, and to the spreading out of the ionization balance caused by hot electrons. Note that higher temperatures and larger fractions of hot electrons are required for reasonable fits of the F- and Mg-like structures for the conical nozzle than for the Laval nozzle. This is in agreement with the recent analyses of Ar plasma from different nozzles. [17,18]

VI. COMPARISON WITH PREVIOUS WORK

In this section, we compare our results for *L*-shell Kr with the results of recent diagnostics of other fs-laser plasmas. Recently [15], *L*-shell emission from a solid Cu target irradiated by an fs-laser pulse was obtained and diagnosed by a kinetics model of O-like through Mg-like Cu. In that case, the laser plasma spectrum was successfully reproduced with a model spectrum at 200 eV with a Maxwellian hot-electron fraction of 10^{-5} . Since Cu has a smaller nuclear charge than Kr, and thus smaller ionization energies for modeled ions, the Ne-like Cu ion has significant population at a bulk plasma temperature of 200 eV, and fractions of hot electrons as small as 10^{-6} increase the relative intensities of F-like to Ne-like emission. The plasma created by an fs-laser pulse on a solid Cu target is also more uniform than the Kr cluster plasma. That homogeneity makes the implementation of opacity straightforward for the Cu plasma, while the inhomogeneous Kr laser plasma presents a challenge for any simple opacity model. Further, the uniform Cu plasma can effectively conduct heat away from the focus of the laser pulse, which leads to a cooler bulk plasma temperature and faster thermalization of hot electrons. The hot electrons in the solid-target fs-laser plasma are thus better described by a Maxwellian distribution than by a Gaussian distribution. Our calculations with a bi-Maxwellian EDF indicate that a Maxwellian hot-electron fraction has effects similar to those of a Gaussian hot-electron fraction one hundred times larger; that is, a bi-Maxwellian EDF with $f=10^{-5}$ gives about the same spectrum as a bulk Maxwellian with a Gaussian hot-electron fraction of 10^{-3} . Given the differences in the models and experiments, it is therefore not surprising that smaller hot-electron fractions and bulk temperatures were found for the solid Cu target than for the Kr gas cluster target.

A closer experimental case for comparison to the current work is given by *K*-shell spectra from 60-fs laser pulses. Such spectra have been well described without opacity by a two-temperature model with a small fraction of Gaussian hot electrons around 10^{-7} – 10^{-4} [16]. The hot-electron fractions and bulk temperatures (150–250 eV) found for Ar clusters irradiated by 60-fs laser pulses are smaller than those found in this work for *L*-shell Kr. Because the ionization energies of Li- and Be-like Ar are smaller than those of Na- and Mg-like Kr, He-like Ar ions have significant populations at bulk plasma temperatures at which Ne-like Kr is only

slightly populated. So while small fractions of hot electrons have significant effects on *K*-shell Ar spectra at a bulk temperature of 200 eV, *L*-shell Kr spectra are affected only by larger fractions of hot electrons.

The significant difference between the diagnosed plasma conditions for similar Ar and Kr experiments is thus clear consequence of the different energies and structures of the *K*-shell and *L*-shell kinetics models. However, there must be some physical cause for the different conditions.

Mathematical modeling of two-phase gas flow [19,25,26] indicates that Kr forms much larger atomic clusters than Ar for the same nozzle type and backing pressure. Larger clusters are less susceptible to destruction by the laser prepulse and are more efficient absorbers of the laser energy, resulting in higher electron temperatures and larger fractions of hot electrons. The effect of cluster size on laser energy absorption efficiency was demonstrated for Ar clusters in Refs. [17] and [18]. Increasing the size of Ar clusters resulted in significant increases in the electron temperatures and hot-electron fractions. For a 35-fs laser pulse incident on relatively large Ar clusters (approximately 10^5 atoms per cluster), fractions of hot electrons on the order of 10^{-2} and electron temperatures around 400 eV were required to describe the observed H-like emission. Those plasma conditions are similar to the ones determined here for a 60-fs laser pulse incident on Kr clusters from the conical nozzle (approximately 10^7 atoms per cluster). The shorter duration of the laser pulse incident on the Ar clusters may compensate for their smaller initial size by depositing its energy before the Ar clusters are destroyed. The dependence of the target absorption efficiency on cluster size is clear, but other distinctions between the Kr and Ar cluster plasmas could be important. The slower expansion of the more massive Kr ions may contribute to the absorption advantage of the larger Kr clusters. And the higher electron densities achievable in larger, more cohesive clusters may contribute to the thermalization of hot electrons, resulting in high electron temperatures in the clusters. More detailed theoretical and experimental work is required to determine the importance of these factors.

VII. SUMMARY AND CONCLUSIONS

The experimental spectra in this paper are the first high-resolution measurements of 4–2 transitions in Kr clusters irradiated by fs-laser pulses with duration shorter than 100 fs. The kinetics model presented here is flexible, incorporating time dependence, hot electrons, and opacity effects. The model is used to isolate a unique set of plasma parameters that accurately describe the spectrum from a ns-laser plasma. Effects of different data sources and coupling schemes have been considered to ensure that the kinetics model is adequate, and because this care has been taken, the importance of opacity on the intensities of Ne-like lines has been established. Further, the same model with hot electrons gives good coincidence with spectra from two different fs-laser experiments and provides strong evidence for the presence of hot electrons in the emitting Kr clusters. The fundamental ideas of fs-laser interaction with atomic clusters that were success-

ful in describing *K*-shell emission from Ar clusters can also be applied to *L*-shell emission from Kr clusters. The inhomogeneity of the gas jet target is evidenced by the presence of narrow Mg-like lines along with broadened Ne- and Na-like lines in the fs-plasma spectra. The formation of a preplasma and the production of a large number of hot electrons in the clusters from their interaction with the main laser pulse are evidenced by the structure of satellite lines and the apparent ionization balance of emitting ions. For gas jets from conical nozzles, we have found that Kr clusters irradiated by a 60-fs laser pulse reach approximately the same conditions as Ar clusters irradiated by a 35-fs laser pulse. This conclusion, while dependent on the accuracy of applied kinetics models, might be useful in the design of future experiments.

ACKNOWLEDGMENTS

The work of S.H. and A.S. was supported in part by the DOE–NNSA/NV Cooperative Agreement DE-FC08-01NV14050, SNL, and UNR. U.I.S. acknowledges partial support by Grant No. B503968 from Lawrence Livermore National Laboratory. The work of K.F. was performed under the auspices of the U.S. Department of Energy by University of California Lawrence Livermore National Laboratory under Contract No. W-7405-Eng-48. This work was also partly supported by the Fond Europeen de Developpement Economique Regional and Conseil Regional d'Aquitaine, NATO Grants Nos. PST.CLG.977637 and CRDF RP1-2328-ME-02.

-
- [1] A. McPherson, T.S. Luk, B.D. Thompson, A.B. Borisov, O.B. Shiryayev, X. Chen, K. Boyer, and C.K. Rhodes, *Phys. Rev. Lett.* **72**, 1810 (1994).
- [2] A. McPherson, B.D. Thompson, A.B. Borisov, K. Boyer, and C.K. Rhodes, *Nature (London)* **370**, 631 (1994).
- [3] T. Ditmire, T. Donnelly, A.M. Rubenchik, R.W. Falcone, and M.D. Perry, *Phys. Rev. A* **53**, 3379 (1996).
- [4] Y.L. Shao, T. Ditmire, J.W.G. Tisch, E. Springate, J.P. Marangos, and M.H.R. Hutchinson, *Phys. Rev. Lett.* **77**, 3343 (1996).
- [5] T. Ditmire, J. Zweiback, V.P. Yanovsky, T.E. Cowan, B. Hays, and K.B. Wharton, *Nature (London)* **398**, 489 (1999).
- [6] M. Lezius, S. Dobosz, D. Normand, and M. Schmidt, *Phys. Rev. Lett.* **80**, 261 (1998).
- [7] S. Dobosz *et al.*, *JETP Lett.* **68**, 485 (1998).
- [8] S. Dobosz *et al.*, *JETP* **88**, 1122 (1999).
- [9] E. Parra, T. Alexeev, J. Fan, K. Kim, S. McNaught, and H. Milchberg, *Phys. Rev. E* **62**, 5931 (2000).
- [10] J. Zweiback, R.A. Smith, T.E. Cowan, G. Hays, K.B. Wharton, V.P. Yanovsky, and T. Ditmire, *Phys. Rev. Lett.* **84**, 2634 (2000).
- [11] H.M. Milchberg, S.J. McNaught, and E. Parra, *Phys. Rev. E* **64**, 056402 (2001).
- [12] A.I. Magunov *et al.*, *JETP Lett.* **74**, 375 (2001).
- [13] J.J. Abdallah, A.Y. Faenov, T.A. Pikuz, M.D. Wilke, G.A. Kyrala, and R.E.H. Clark, *J. Quant. Spectrosc. Radiat. Transf.* **62**, 1 (1999).
- [14] J. Abdallah, Jr., A.Y. Faenov, D. Hammer, S. Pikuz, G. Csanak, and R.E.H. Clark, *Phys. Scr.* **53**, 705 (1996).
- [15] K. Fournier *et al.*, LLNL Report No. UCRL-146633 2002 (unpublished).
- [16] J. Abdallah, A.Y. Faenov, I.Y. Skobelev, A.I. Magunov, T.A. Pikuz, T. Augustine, P. D'Oliveira, S. Hulin, and P. Monot, *Phys. Rev. A* **63**, 032706 (2001).
- [17] G.C. Junkel-Vives, J. Abdallah, F. Blasco, C. Stenz, F. Salin, A.Y. Faenov, A.I. Magunov, T.A. Pikuz, and I.Y. Skobelev, *Phys. Rev. A* **64**, 021201(R) (2001).
- [18] G.C. Junkel-Vives *et al.*, *J. Quant. Spectrosc. Radiat. Transf.* **71**, 417 (2001).
- [19] G.C. Junkel-Vives *et al.*, *Phys. Rev. E* **65**, 036410 (2002).
- [20] G. C. Junkel-Vives *et al.*, *Phys. Rev. A* **66**, 033204 (2002).
- [21] J.J. Abdallah, R.E.H. Clark, A.Y. Faenov, L. Karpinski, S.A. Pikuz, V.M. Romanova, M. Sadowski, M. Sholz, and A. Szydłowski, *J. Quant. Spectrosc. Radiat. Transf.* **62**, 85 (1999).
- [22] C. Stenz, V. Bagnoud, F. Blasco, J.R. Roche, F. Salin, A.Y. Faenov, A.I. Magunov, T.A. Pikuz, and I.Y. Skobelev, *Quantum Electron.* **30**, 721 (2000).
- [23] F. Blasco, C. Stenz, F. Salin, A.Y. Faenov, A.I. Magunov, T.A. Pikuz, and I.Y. Skobelev, *Rev. Sci. Instrum.* **72**, 1956 (2001).
- [24] T. Augustine, P. D'Oliveira, S. Hulin, P. Monot, J.J. Abdallah, A.Y. Faenov, I.Y. Skobelev, A.I. Magunov, and T.A. Pikuz, *JETP Lett.* **72**, 38 (2000).
- [25] A.S. Boldarev, V.A. Gasilov, F. Blasco, C. Stenz, F. Dorchies, F. Salin, A.Y. Faenov, T.A. Pikuz, A.I. Magunov, and I.Y. Skobelev, *JETP Lett.* **73**, 514 (2001).
- [26] I.Y. Skobelev *et al.*, *JETP* **94**, 73 (2002).
- [27] I. Yu. Skobelev *et al.*, *JETP* **94**, 966 (2002).
- [28] A.Y. Faenov, S.A. Pikuz, A.I. Erko, B.A. Bryunetkin, V.M. Dyakin, G.V. Ivanenkov, A.R. Mingaleev, T.A. Pikuz, V.M. Romanova, and T.A. Shelkovenko, *Phys. Scr.* **50**, 333 (1994).
- [29] I.Y. Skobelev, A.Y. Faenov, B.A. Bryunetkin, V.M. Dyakin, T.A. Pikuz, S.A. Pikuz, T.A. Shelkovenko, V.M. Romanova, and A.R. Mingaleev, *JETP* **81**, 692 (1995).
- [30] T.A. Pikuz, A.Y. Faenov, S.A. Pikuz, V.M. Romanova, and T.A. Shelkovenko, *J. X-Ray Sci. Technol.* **5**, 323 (1995).
- [31] B.K.F. Young *et al.*, *Rev. Sci. Instrum.* **69**, 4049 (1998).
- [32] V.M. Dyakin, I.Y. Skobelev, A.Y. Faenov, A. Bartnik, H. Fiedorowicz, M. Szczurek, A. Osterheld, and J. Nilsen, *Quantum Electron.* **27**, 691 (1997).
- [33] J.E. Rice, K.B. Fournier, J.A. Goetz, E.S. Marmar, and J.L. Terry, *J. Phys. B* **33**, 5435 (2000).
- [34] E. Biemont, Y. Fremat, and P. Quinet, *At. Data Nucl. Data Tables* **71**, 117 (1999).
- [35] T. A. Carlson, J. C. W. Nestor, N. Wasserman, and J. D. McDowell, Oak Ridge National Laboratory Report No. 4562 1970 (unpublished).
- [36] V.A. Bernshtam, Y.V. Ralchenko, and Y. Maron, *J. Phys. B* **33**, 5025 (2000).
- [37] V. P. Shevelko, *Atoms and Their Spectroscopic Properties* (Springer-Verlag, Berlin, 1997).
- [38] R. D. Cowan, *The Theory of Atomic Structure and Spectra* (University of California Press, Berkeley, 1981).
- [39] U.I. Safronova, C. Namba, I. Murakami, W.R. Johnson, and

- M.S. Safronova, Phys. Rev. A **64**, 012507 (2001).
- [40] H.V. Regemorter, Astrophys. J. **136**, 906 (1962).
- [41] H. Sampson, H.L. Zhang, and C.J. Fontes, At. Data Nucl. Data Tables **48**, 25 (1991).
- [42] H.L. Zhang, D.H. Sampson, R.E. Clark, and J.B. Mann, At. Data Nucl. Data Tables **37**, 17 (1987).
- [43] H.L. Zhang, D.H. Sampson, R.E. Clark, and J.B. Mann, At. Data Nucl. Data Tables **41**, 1 (1989).
- [44] A. Dasgupta, K.G. Whitney, H.L. Zhang, and D.H. Sampson, Phys. Rev. E **55**, 3460 (1997).
- [45] W.H. Goldstein, B.L. Whitten, A.U. Hazi, and M.H. Chen, Phys. Rev. A **36**, 3607 (1987).
- [46] O. Peyrusse, P. Combis, M. Louis-Jacquet, D. Naccache, C.J. Keane, B.J. McGowan, and D.L. Matthews, J. Appl. Phys. **65**, 3802 (1989).
- [47] U. Feldman, J.F. Seely, and A.K. Bhatia, J. Appl. Phys. **58**, 3954 (1985).
- [48] M. Klapisch, J.L. Schwob, B.S. Fraenkel, and J. Oreg, J. Opt. Soc. Am. **67**, 148 (1977).
- [49] A. Bar-Shalom, M. Klapisch, and J. Oreg, Phys. Rev. A **38**, 1773 (1988).
- [50] V.A. Boiko, S.A. Pikuz, I.Y. Skobelev, and A.Y. Faenov, J. Sov. Laser Res. **6**, 85 (1985).
- [51] K. B. Fournier *et al.* (unpublished).